INTERNATIONAL JOURNAL FOR NUMERICAL METHODS IN FLUIDS
Int. J. Numer. Meth. Fluids 2010; **62**:927–944
Published online 1 April 2009 in Wiley InterScience (www.interscience.wiley.com). DOI: 10.1002/fld.2048

A well-balanced upstream flux-splitting finite-volume scheme for shallow-water flow simulations with irregular bed topography

Jihn-Sung Lai[1,*,†], Wen-Dar Guo[1], Gwo-Fong Lin[2] and Yih-Chi Tan[1,3]

[1]*Hydrotech Research Institute, National Taiwan University, Taipei 10617, Taiwan*
[2]*Department of Civil Engineering, National Taiwan University, Taipei 10617, Taiwan*
[3]*Department of Bioenvironmental Systems Engineering, National Taiwan University, Taipei 10617, Taiwan*

SUMMARY

This study extends the upstream flux-splitting finite-volume (UFF) scheme to shallow water equations with source terms. Coupling the hydrostatic reconstruction method (HRM) with the UFF scheme achieves a resultant numerical scheme that adequately balances flux gradients and source terms. The proposed scheme is validated in three benchmark problems and applied to flood flows in the natural/irregular river with bridge pier obstructions. The results of the simulations are in satisfactory agreement with the available analytical solutions, experimental data and field measurements. Comparisons of the present results with those obtained by the surface gradient method (SGM) demonstrate the superior stability and higher accuracy of the HRM. The stability test results also show that the HRM requires less CPU time (up to 60%) than the SGM. The proposed well-balanced UFF scheme is accurate, stable and efficient to solve flow problems involving irregular bed topography. Copyright © 2009 John Wiley & Sons, Ltd.

Received 3 February 2008; Revised 9 January 2009; Accepted 6 February 2009

KEY WORDS: upstream flux-splitting finite-volume scheme; shallow water equations; hydrostatic reconstruction method; surface gradient method; bridge pier obstructions; well balanced

1. INTRODUCTION

Currently, the two-dimensional (2D) shallow water equations (SWE) are solved usually using the high-resolution shock-capturing schemes implemented by the finite volume method (FVM) [1–4]. Unfortunately, these schemes can cause problematic stability/convergence in cases of non-homogeneous equations due to imbalance between flux gradients and source terms [5]. In turn, the source terms arise in the SWE as a result of variable bed topography, and handling of these terms presents today a challenge for hydraulic calculation of rivers. Therefore, there is a need to

*Correspondence to: Jihn-Sung Lai, Hydrotech Research Institute, National Taiwan University, Taipei 10617, Taiwan.
†E-mail: jslai525@ntu.edu.tw

Contract/grant sponsor: National Science Council; contract/grant number: NSC 96-2625-Z-002-013

develop a new class of numerical schemes that would deal with the non-homogeneous terms in SWE with higher accuracy and better robustness.

The main difficulty in treating source terms is to properly balance the source terms with the flux gradients. Several works [6–8] have used the fractional step method to split the non-homogeneous SWE into homogeneous parts and source terms. Although the fractional step method can be implemented easily, it induces numerical instability and errors in cases of steady flow with bed-slope variations [8]. Therefore, several numerical methods for the correct treatment of source terms have been proposed to construct so-called 'well-balanced' schemes [9–15]. A numerical scheme is said to be well-balanced if it can preserve steady-state solutions in which the source terms are exactly balanced by flux gradients [9]. Zhou *et al.* [16, 17] proposed a surface gradient method (SGM) and compared it with the depth gradient method (DGM). Audusse *et al.* [18] proposed a hydrostatic reconstruction method (HRM) for dealing with the source terms. Compared with other methods [14, 15], HRM coding is easier since the Jacobian matrix is not used in the calculation algorithm [19].

In the present study, the upstream flux-splitting finite-volume (UFF) scheme proposed by Lai *et al.* [20] is adopted to estimate the numerical flux through each cell interface. In the treatment of source terms, the HRM is employed to prevent the imbalance between flux gradients and source terms. The UFF scheme is then coupled with the HRM, which has never been done before and for this reason the new scheme is of interest. The three shallow-water flow simulations include steady flow over an irregular bed, dam-break flow over two humps and still water over a 2D symmetric hump. The simulation results obtained using the DGM and SGM are also presented for comparison. Finally, simulations of typhoon flood flows around bridge piers are performed and compared with field-measured water levels in the river.

2. GOVERNING EQUATIONS

The set of 2D SWE with source terms expressed in the differential conservative form is [21]

$$\frac{\partial \mathbf{Q}}{\partial t}+\frac{\partial \mathbf{F}}{\partial x}+\frac{\partial \mathbf{G}}{\partial y}=\mathbf{S} \tag{1}$$

in which

$$\mathbf{Q}=\begin{bmatrix} h \\ hu \\ hv \end{bmatrix}, \quad \mathbf{F}=\begin{bmatrix} hu \\ hu^2+\dfrac{gh^2}{2} \\ huv \end{bmatrix}, \quad \mathbf{G}=\begin{bmatrix} hv \\ huv \\ hv^2+\dfrac{gh^2}{2} \end{bmatrix}, \quad \mathbf{S}=\begin{bmatrix} 0 \\ gh(s_{0x}-s_{fx}) \\ gh(s_{0y}-s_{fy}) \end{bmatrix} \tag{2}$$

where $\mathbf{Q}$ is the vector of conserved variables, $\mathbf{F}$ and $\mathbf{G}$ are the flux vectors in the x- and y-directions, respectively, h is the water depth, u and v are the depth-averaged velocity components in the x- and y-directions, respectively, g is the acceleration due to gravity, $\mathbf{S}$ is the source-term vector, $s_{0x}=-\partial z_b/\partial x$ and $s_{0y}=-\partial z_b/\partial y$ are the bed slopes in the x- and y-directions, respectively, z_b is the bed elevation, and s_{fx} and s_{fy} are the friction slopes in the x- and y-directions, respectively.

DOI: 10.1002/fld

The Manning formula is adopted herein to estimate the friction slopes, which are defined as

$$s_{fx}=\frac{un_m^2\sqrt{u^2+v^2}}{h^{4/3}},\quad s_{fy}=\frac{vn_m^2\sqrt{u^2+v^2}}{h^{4/3}} \tag{3}$$

where n_m is Manning's roughness coefficient (see [22]).

3. NUMERICAL FORMULATIONS

3.1. Numerical discretization by FVM

In the framework of FVM, the integral form of 2D SWE over the control volume Ω is written as [21]

$$\iint_\Omega \frac{\partial \mathbf{Q}}{\partial t}\,\mathrm{d}W+\int_{\partial\Omega}\mathbf{E}\cdot\mathbf{n}\,\mathrm{d}l=\iint_\Omega \mathbf{S}\,\mathrm{d}W \tag{4}$$

in which $\mathbf{n}$ is the outward unit vector normal to the boundary $\partial\Omega$, $\mathrm{d}W$ and $\mathrm{d}l$ are the area and arc elements, respectively, and the integrand $\mathbf{E}\cdot\mathbf{n}$ is the normal flux vector in which $\mathbf{E}=[\mathbf{F},\mathbf{G}]^{\mathrm{T}}$ The conserved variables $\mathbf{Q}$ are cell-averaged within the control volumes and then the basic vector equation of FVM becomes

$$\frac{\mathrm{d}\mathbf{Q}}{\mathrm{d}t}+\frac{1}{A}\sum_{m=1}^{M}\mathbf{E}_n^m L^m=\frac{1}{A}\iint_\Omega \mathbf{S}\,\mathrm{d}W \tag{5}$$

where A is the area of a cell, m is the index of a cell edge, M is the total number of cell edges, L^m is the length of a edge and $\mathbf{E}_n^m$ is the normal flux across edge m separating two neighboring cells. In turn, the flux $\mathbf{E}_n^m$ can be determined from the rotational invariance property of the governing equations [23]:

$$\mathbf{E}_n(\mathbf{Q})=\mathbf{F}\cos\theta+\mathbf{G}\sin\theta=\mathbf{T}(\theta)^{-1}\mathbf{F}(\overline{\mathbf{Q}})=\mathbf{T}(\theta)^{-1}\mathbf{F}[\mathbf{T}(\theta)\mathbf{Q}] \tag{6}$$

where θ is the angle between the outward unit vector $\mathbf{n}$ and x-axis, $\overline{\mathbf{Q}}=[h,hu_n,hv_t]^{\mathrm{T}}$ is the vector transformed from $\mathbf{Q}$, $\mathbf{F}(\overline{\mathbf{Q}})=[hu_n,hu_n^2+gh^2/2,hu_nv_t]^{\mathrm{T}}$ is the transformed normal flux, u_n and v_t are respectively the flow velocity components in $\bar{x}$(normal) and $\bar{y}$(tangential) directions, which are $u_n=u\cos\theta+v\sin\theta$ and $v_t=v\cos\theta-u\sin\theta$, and $\mathbf{T}(\theta)$ and $\mathbf{T}(\theta)^{-1}$ are the transformation matrix and its inverse, respectively:

$$\mathbf{T}(\theta)=\begin{bmatrix}1&0&0\\0&\cos\theta&\sin\theta\\0&-\sin\theta&\cos\theta\end{bmatrix},\quad \mathbf{T}(\theta)^{-1}=\begin{bmatrix}1&0&0\\0&\cos\theta&-\sin\theta\\0&\sin\theta&\cos\theta\end{bmatrix} \tag{7}$$

Combining Equations (5) and (6) gives

$$\frac{\mathrm{d}\mathbf{Q}}{\mathrm{d}t}+\frac{1}{A}\sum_{m=1}^{M}\mathbf{T}(\theta)^{-1}\mathbf{F}(\bar{\mathbf{Q}})L^m=\frac{1}{A}\iint_\Omega \mathbf{S}\,\mathrm{d}W \tag{8}$$

In the framework of FVM, the 2D problem formulated in Equation (8) is simplified into the series of 1D local problem in the direction normal to the cell interface. Owing to the discontinuities at the cell interface, the estimation of the normal flux $\mathbf{F}(\overline{\mathbf{Q}})$ at each cell interface can be referred to

DOI: 10.1002/fld

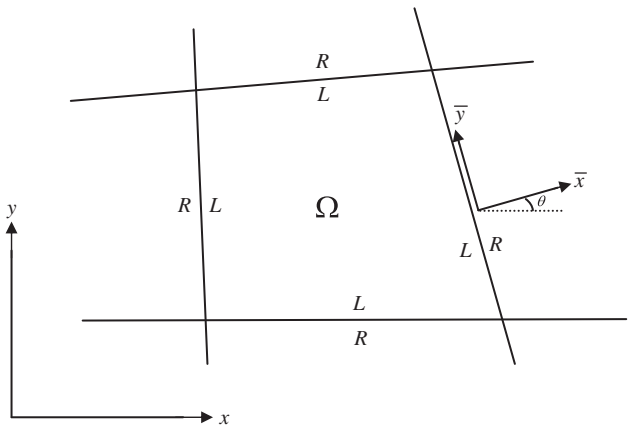

Figure 1. The finite-volume cell Ω and its cell interface.

the local 1D Riemann problem, which can be written in vector form as [24]

$$\frac{\partial \bar{\mathbf{Q}}}{\partial t} + \frac{\partial [\mathbf{F}(\bar{\mathbf{Q}})]}{\partial \bar{x}} = 0 \tag{9a}$$

with the initial condition

$$\bar{\mathbf{Q}}(\bar{x}, 0) = \begin{cases} \bar{\mathbf{Q}}_L, & \bar{x} < 0 \\ \bar{\mathbf{Q}}_R, & \bar{x} > 0 \end{cases} \tag{9b}$$

where $\bar{x}$ is the transformed x-axis (see Figure 1). Here, the subscripts L and R represent values of a variable in the left and right cells with respect to the interface LR.

The homogeneous part of Equation (8) is discretized using the Euler method [23] as follows:

$$\mathbf{Q}^{n+1} = \mathbf{Q}^n - \frac{\Delta t}{A}\left[\sum_{m=1}^{M} \mathbf{T}(\theta)^{-1}\mathbf{F}(\bar{\mathbf{Q}})L^m\right] + \frac{\Delta t}{A}\iint_{\Omega} \mathbf{S}\,\mathrm{d}W \tag{10}$$

where n is the time index and Δt is the time increment.

3.2. UFF scheme

The UFF scheme proposed by Lai *et al.* [20] is employed to estimate the numerical flux $\mathbf{F}(\bar{\mathbf{Q}}) = \mathbf{F}_{LR}(\bar{\mathbf{Q}}_L, \bar{\mathbf{Q}}_R)$ through each cell interface.

According to the work of Lai *et al.* [20], the flux vector $\mathbf{F}(\bar{\mathbf{Q}})$ is splitted into two parts $(\mathbf{F}_{LR,1}, \mathbf{F}_{LR,2})$ by introducing two wave speeds (s_1, s_2):

$$\mathbf{F}_{LR}(\bar{\mathbf{Q}}_L, \bar{\mathbf{Q}}_R) = \frac{-s_2}{s_1 - s_2}\mathbf{F}_{LR,1} + \frac{s_1}{s_1 - s_2}\mathbf{F}_{LR,2} \tag{11}$$

Using the Steger–Warming approach [24], the numerical flux $\mathbf{F}_{LR,1}$ is expressed as

$$\mathbf{F}_{LR,1} = \tfrac{1}{2}(\mathbf{P}_L + \mathbf{P}_R) + \Delta\bar{\mathbf{Q}}_{av} \tag{12}$$

DOI: 10.1002/fld

where $\mathbf{P}=[0, p, 0]^{\mathrm{T}}$ is the pressure component, $p=gh^2/2$ is the hydrostatic pressure contribution and the term $\Delta\bar{\mathbf{Q}}_{av}$ represents the numerical viscosity, which is given by

$$\Delta\bar{\mathbf{Q}}_{av}=\frac{1}{2\max(c_L,c_R)}\begin{bmatrix}p_L-p_R\\(pu_n)_L-(pu_n)_R\\(pv_t)_L-(pv_t)_R\end{bmatrix} \tag{13}$$

where $c=\sqrt{gh}$ is the local wave celerity. Using the upwind approach, the numerical flux $\mathbf{F}_{LR,2}$ is given by

$$\mathbf{F}_{LR,2}=[(u_n)_{L/R}-s_2]\bar{\mathbf{Q}}_{L/R}+\mathbf{P}_{L/R} \tag{14}$$

where the subscript L/R is defined as

$$L/R=\begin{cases}L & \text{if } s_1>0\\ R & \text{if } s_1\leqslant 0\end{cases} \tag{15}$$

The values of s_1 and s_2 can be computed from

$$s_1=\tfrac{1}{2}[(u_n)_L+(u_n)_R] \tag{16a}$$

$$s_2=\begin{cases}\min[0,(u_n)_L-c_L,u_n^*-c^*] & \text{if } s_1>0\\ \max[0,(u_n)_R+c_R,u_n^*+c^*] & \text{if } s_1\leqslant 0\end{cases} \tag{16b}$$

in which u_n^* and c^* is estimated using the exact solutions given by Toro [23]:

$$u_n^*=\tfrac{1}{2}[(u_n)_L+(u_n)_R]+c_L-c_R \tag{17a}$$

$$c^*=\tfrac{1}{2}(c_L+c_R)+\tfrac{1}{4}[(u_n)_L-(u_n)_R] \tag{17b}$$

The detailed description of the UFF scheme is given in [20].

3.3. Treatment of source terms

According to the HRM, the transformed conserved variables are reconstructed as

$$\bar{\mathbf{Q}}^{\mathrm{HRM}}_{LR-}=\begin{bmatrix}h^{\mathrm{HRM}}_{LR-}\\ h^{\mathrm{HRM}}_{LR-}(u_n)_L\\ h^{\mathrm{HRM}}_{LR-}(v_t)_L\end{bmatrix},\quad \bar{\mathbf{Q}}^{\mathrm{HRM}}_{LR+}=\begin{bmatrix}h^{\mathrm{HRM}}_{LR+}\\ h^{\mathrm{HRM}}_{LR+}(u_n)_L\\ h^{\mathrm{HRM}}_{LR+}(v_t)_L\end{bmatrix} \tag{18}$$

Following the work of Audusse *et al*. [18, 19], the hydrostatic reconstructed water depth on each edge of the considered interface is represented as

$$h^{\mathrm{HRM}}_{LR-}=\max[0,h_L+(z_b)_L-(z_b)_{LR}],\quad h^{\mathrm{HRM}}_{LR+}=\max[0,h_R+(z_b)_R-(z_b)_{LR}] \tag{19}$$

in which $(z_b)_{LR}$ is the interface bed elevation value. To ensure that the water height during a simulation stays always positive, the interface bed elevation is defined in an upwind evaluation form

$$(z_b)_{LR}=\max[(z_b)_L,(z_b)_R] \tag{20}$$

DOI: 10.1002/fld

In the presented framework of FVM, the numerical bed-slope source-term discretization can be easily added into the numerical flux function as expressed in Equation (11). Owing to the rotational invariance property of SWE, only the x component of the bed-slope source terms should be added into numerical flux, which is modified as

$$\mathbf{F}(\bar{\mathbf{Q}})=\mathbf{F}_{LR}(\bar{\mathbf{Q}}_{LR-}^{\mathrm{HRM}},\bar{\mathbf{Q}}_{LR+}^{\mathrm{HRM}})+\begin{pmatrix}0\\ \dfrac{g}{2}h_L^2-\dfrac{g}{2}(h_{LR-}^{\mathrm{HRM}})^2\\ 0\end{pmatrix} \tag{21}$$

Equation (21) shows that the reconstructed values $\bar{\mathbf{Q}}_{LR-}^{\mathrm{HRM}}$ and $\bar{\mathbf{Q}}_{LR+}^{\mathrm{HRM}}$ expressed in Equation (18) are respectively used instead of $\bar{\mathbf{Q}}_L$ and $\bar{\mathbf{Q}}_R$ to compute the interface numerical flux in the UFF scheme. Finally, only the friction-slope source terms in the inhomogeneous part need to be discretized as

$$\frac{\Delta t}{A}\left(\int\!\!\int_{\Omega}\mathbf{S}\,\mathrm{d}W\right)_x=-g\Delta t\frac{un_m^2\sqrt{u^2+v^2}}{h^{1/3}},\quad \frac{\Delta t}{A}\left(\int\!\!\int_{\Omega}\mathbf{S}\,\mathrm{d}W\right)_y=-g\Delta t\frac{vn_m^2\sqrt{u^2+v^2}}{h^{1/3}} \tag{22}$$

3.4. Stability and boundary conditions

The Courant–Friedrichs–Lewy (CFL) condition for the UFF scheme has to be imposed to ensure the numerical stability [25, 26]:

$$\mathrm{CFL}=\frac{\Delta t}{\min(d_{LR})}\max(\sqrt{u^2+v^2}+c)\leqslant 1 \tag{23}$$

where d_{LR} indicates the distances between the cell L and the cell R.

Boundary conditions are of two different types: the land boundary and the open boundary. For the land boundary, the velocity normal to the land is set to zero (i.e. $h_R=h_L, u_{nR}=-u_{nL}, v_{tR}=v_{tL}$). The open boundary is set by making use of the outgoing Riemann invariants. For more details see [25, 26].

4. NUMERICAL RESULTS AND DISCUSSIONS

The numerical performance of the well-balanced UFF scheme is evaluated by simulating several well-known benchmark problems, including steady flow over an irregular bed, dam-break flow over two humps and steady flow over a 2D symmetric hump. The numerical accuracy of the scheme is evaluated by comparing the results with exact solutions using the error norms of E_1 and E_2 defined as follows [27]:

$$E_1=\frac{\sum|Y^{\mathrm{sim}}-Y^{\mathrm{exact}}|}{\sum|Y^{\mathrm{exact}}|},\quad E_2=[\sum(Y^{\mathrm{sim}}-Y^{\mathrm{exact}})^2]^{1/2} \tag{24}$$

where Y^{sim} and Y^{exact} are simulated and exact results respectively at each computed cell. Note that the exact solution in Equation (24) is analytical or experimental depending on the flow case. Those by HRM to some simulations are carried out using SGM [16] and DGM [16] for comparison purposes. Finally, the applicability of the proposed well-balanced scheme is demonstrated by flood

DOI: 10.1002/fld

Table I. Definition of the bed variations for steady flow over an irregular bed.

x (m)	0	50	100	150	250	300	350	400	425	435	450	475	500	505
z_b (m)	0	0	2.5	5	5	3	5	5	7.5	8	9	9	9.1	9
x (m)	530	550	565	575	600	650	700	750	800	820	900	950	1000	1500
z_b (m)	9	6	5.5	5.5	5	4	3	3	2.3	2	1.2	0.4	0	0

flow simulations in the river reach with irregular bed topography. All simulations were performed on a Pentium IV 2.2 GHz computer equipped with 1 GB RAM.

4.1. Steady flow over an irregular bed

To demonstrate the applicability of the proposed scheme to solve channel flow with strong variations of bottom topography, a steady flow in a 1500 m long and 1 m wide rectangular channel is tested herein as a benchmark problem. This test case can provide a good insight into numerical performance. The bed topography is described in Table I and shown in Figure 2(a). The same bed topography was also used earlier by Zhou *et al.* [16] and by Tseng [28]. A discharge of $0.75\,m^2/s$ per unit width is imposed at the upstream boundary (i.e. $x=0$ m) and water depth of 15 m is specified at the downstream boundary (i.e. $x=1500$ m). The Manning roughness coefficient is set to 0.1. Two hundred uniform cells are used. The computational time step is 0.08 s.

Figures 2(a), (b) and (c) show the simulated water levels, velocities and discharges per unit width, respectively, in comparison with exact solutions. If the well-balanced property of a scheme is preserved, the water level should be in a state of equilibrium (i.e. water level should remain at 15 m) and the discharge should be constant (i.e. discharge should remain at $0.75\,m^2/s$) [28]. The simulation results show that the source-term treatment by DGM produces significantly large numerical errors due to the reconstruction of water depth at the cell interface. The results also indicate that the well-balanced property of HRM and SGM does improve numerical accuracy. The close-up of simulated discharges in Figure 2(c), for example, indicates that HRM produces better resolution than SGM does. Table II summarizes the E_1 norms and CPU times required to achieve convergence. These data are used to quantitatively evaluate overall numerical accuracy as well as efficiency. The data in Table II reveal that the HRM resulting in smaller E_1 norms is more accurate than the SGM, and that the SGM is about 14% more expensive than the HRM in terms of CPU-time consumption. Consequently, the proposed scheme with HRM is the most accurate and efficient among the presented methods. The DGM obtains most inaccurate solutions so that it is not used for the other applications in the following sections.

4.2. Dam-break flow over two humps

To assess the capability of the proposed scheme for dam-break flow problems involving irregular bed slope, data from experiments conducted by Aureli *et al.* [29] are adopted. Figure 3 shows the schematic of the experiment consisting of a rectangular reservoir connected to a 1 m wide channel with two humps. The experimental series are focused on setting different upstream water levels and different numbers of humps to induce the rarefaction waves, shock waves and reverse flows in the flow field. Two test cases of experiments are considered herein. Test case 1 is the flow running over hump 1 with an initial upstream water level of 0.35 m. Test case 2 is the flow propagating over both humps 1 and 2 with an initial upstream water level of 0.45 m. Both test cases have the

DOI: 10.1002/fld

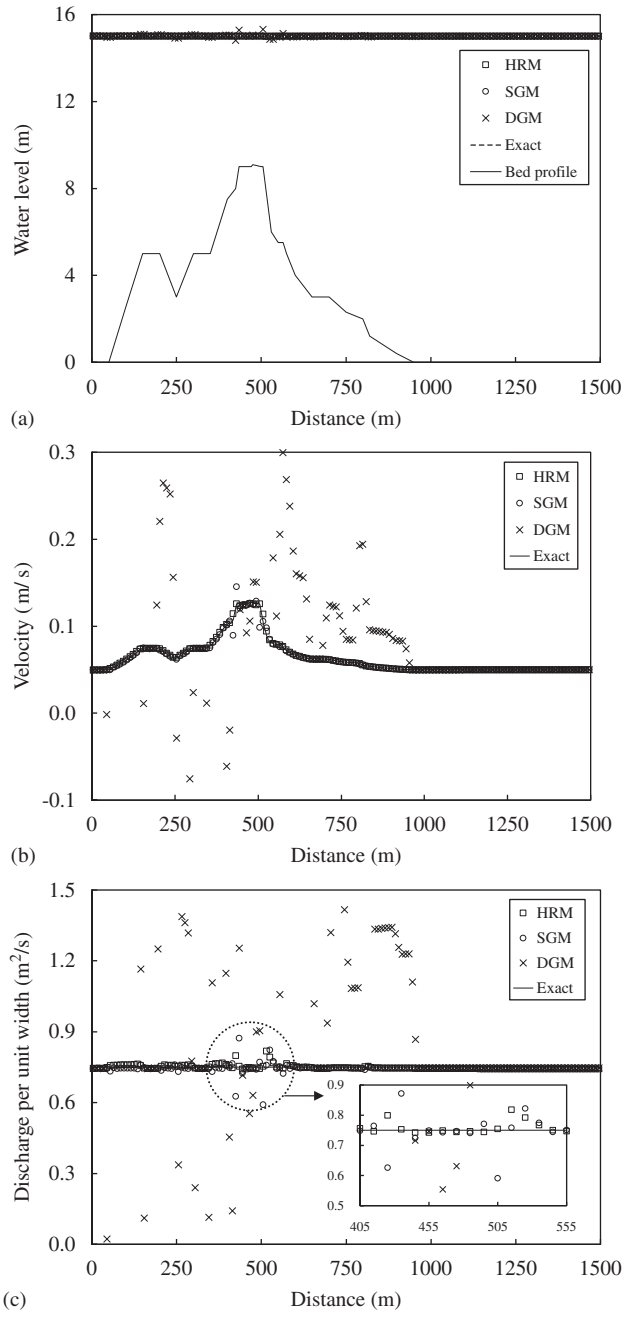

Figure 2. Comparisons of exact solutions with simulated (a) water level; (b) velocity; and (c) discharge per unit width for the steady flow over an irregular bed.

DOI: 10.1002/fld

Table II. The E_1 norms and CPU time for the steady flow over an irregular bed.

Treatments of source terms	E_1 of the water level	E_1 of the velocity	E_1 of the discharge per unit width	CPU for convergence (s)
HRM	1.47×10^{-4}	1.05×10^{-2}	0.99×10^{-2}	0.893
SGM	1.91×10^{-4}	1.51×10^{-2}	1.11×10^{-2}	1.015

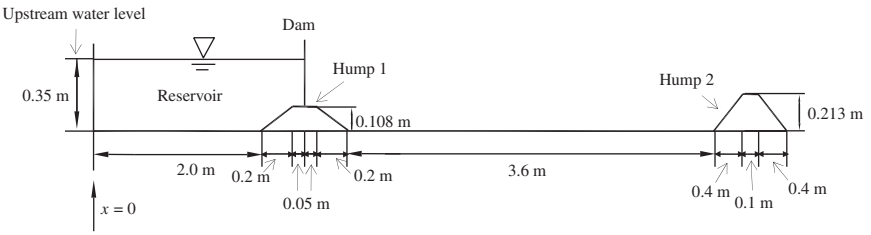

Figure 3. Layout of the dam-break experiment over two humps.

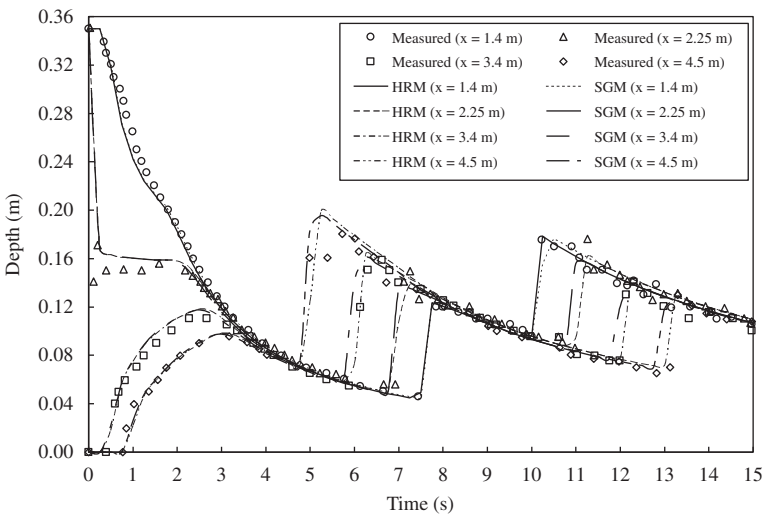

Figure 4. Comparisons of the measured and simulated results for the test case 1 of the dam-break experiment over one hump.

initial downstream water depth of 0 m. The Manning roughness coefficient is set to 0.01, which is the value adopted in Aureli *et al.* [29]. The walls and the upstream end of the channel are set as the land boundary conditions. A transmissive boundary condition [23] is set at the downstream end of the channel. The computational mesh with 140 uniform cells is used and the computational time step is 0.02 s. The total simulation time is 15 s.

For the test case 1 with hump 1, Figure 4 compares the measured and simulated water-depth hydrographs. For all observation stations at $x = 1.4$, 2.25, 3.4 and 4.5 m, the simulated results

DOI: 10.1002/fld

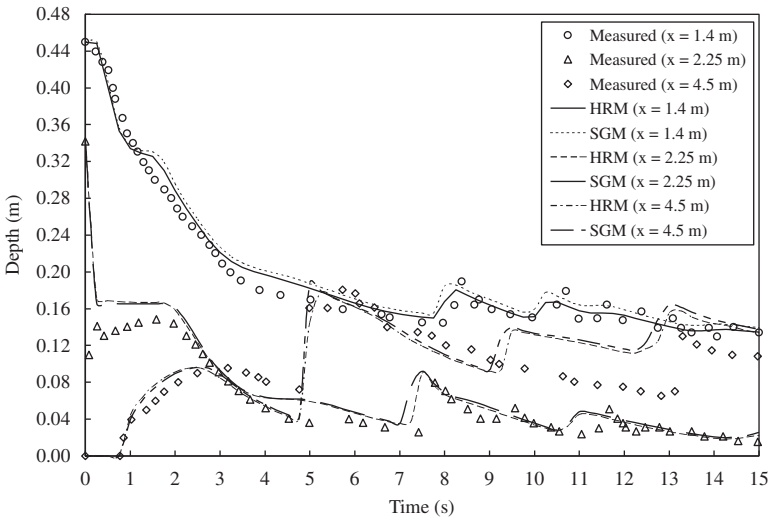

Figure 5. Comparisons of the measured and simulated results for the test case 2 of the dam-break experiment over two humps.

including the shocks, the dry/wet fronts and the reverse flows agree closely with the measured. For the test case 2 (two humps), the solution is shown in Figure 5. One can see from the figure that the HRM and SGM simulations reveal similar trends in the water-depth hydrographs. However, the HRM method appears to provide sharper resolution of shocks than that by SGM. Moreover, the SGM requires 14% more CPU time than the HRM.

4.3. Still water over a 2D symmetric hump

Still-water flow over a 2D symmetric hump is a common benchmark test (see [14, 30]), and it is simulated here to assess. The numerical experiment is performed in a 1 m square pool. In the center of the pool, there is a symmetric hump at the bottom defined as follows:

$$z_b(x, y) = \max\{0, 0.25 - 5[(x-0.5)^2 + (y-0.5)^2]\} \tag{25}$$

Figure 6 shows the simulation domain with the defined bed elevation contours [14, 30] and the unstructured mesh of 2020 cells. As $t=0$, the water is still ($u=0$), whereas the water level in the pool is 0.5 m. Naturally, the exact solution for this problem is $u=0$ for $t>0$. The computational time step is 0.01 s.

The HRM simulation results reveal no change in the velocity field and the still-water state is maintained. For comparison, Figure 7 plots the 2D contours of water depth and the velocity fields computed by SGM. Although the SGM is a well-balanced treatment of source terms, it produces spurious velocity field (see Figure 7) with the maximum velocity of 0.016 m/s. This is a consequence of central bed-slope discretization in the SGM. We note that the spurious velocities decrease with refining the computational mesh. For instance, a simulation using a grid of 4040 cells also resulted in a spurious velocity field, but with the maximum velocity of 0.005 m/s. Nevertheless, spurious velocities may cause the problem of numerical instability.

DOI: 10.1002/fld

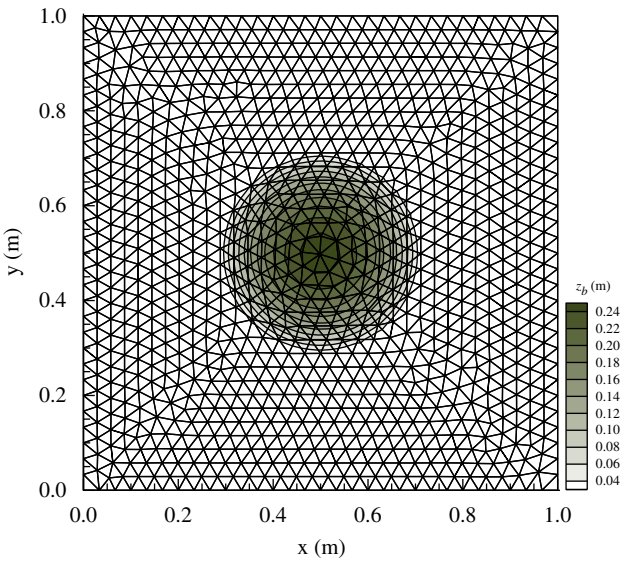

Figure 6. Unstructured mesh and bed elevation contours in still-water flow simulation over a symmetric hump.

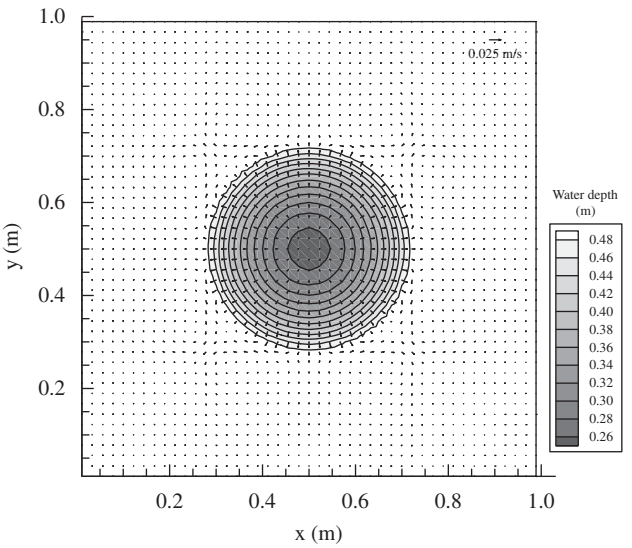

Figure 7. 2D simulated water depths and velocity field using SGM for still-water flow simulation over a symmetric hump.

To find the stability limits of the HRM and SGM schemes, an additional test is performed, in which the same mesh of 2020 cells is employed, but the time step is consecutively increased until the simulation goes unstable. The results are given in Table III. The maximum allowable time steps

DOI: 10.1002/fld

Table III. The E_2 norms and time step for still water over a 2D symmetric hump.

Treatments of source terms	E_2 of water level	E_2 of velocity	Allowable time step (s)
HRM	3.87×10^{-4}	6.71×10^{-4}	0.023
SGM	3.11×10^{-3}	3.06×10^{-2}	0.017

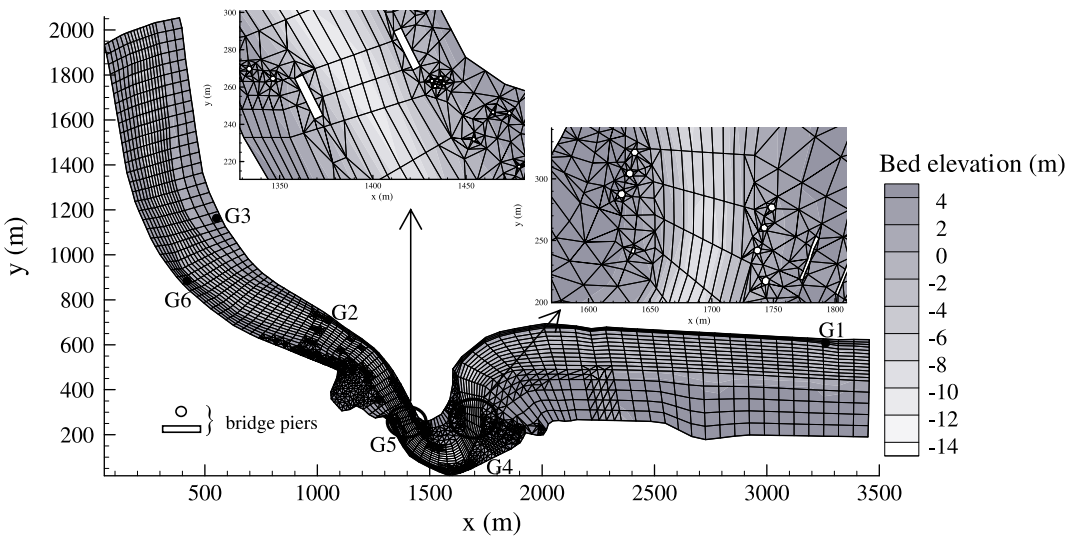

Figure 8. Computational mesh with bed elevation contours and six water-level gauge stations for the 2D flood flow simulations in the study reach.

for the two schemes are 0.023 and 0.017 s, respectively. Therefore, from the perspective of CPU time the SGM scheme is 24% more expensive than the HRM, whereas the accuracy of the results obtained using the HRM are higher than that of SGM (see table). Consequently, the HRM provides better numerical accuracy and stability in the 2D still-water flow with variable bed topography.

4.4. Flood flows around bridge piers

The well-balanced UFF scheme is applied to the simulation of flood propagation in the 2D irregular bed topography, for which the field-measured water levels are available at six gauges [31]. The study area is the Yuanshan reach of the Keelung River, which is a major tributary of the Tamshui River in northern Taiwan. This reach is confined by vertical-walled levees and has a significant-narrow bend and irregular bed variations between the main river channel and the floodplain. Moreover, hydraulic structures in the form of bridge piers are presented in the reach being considered.

Figure 8 shows the computational mesh that includes 1576 quadrilateral and 2951 triangular cells. It also shows the bed elevations that range from 14 m below sea level to 4 m above sea level. Six water-level gauge stations provide the field-measured water level [31] data required for Manning coefficient calibration and numerical verification. The gauge stations G1, G2 and G3 are located on the right bank, and G4, G5 and G6 are located on the left bank. Keelung River flooding

DOI: 10.1002/fld

usually results from heavy rainfall during typhoon events, the following two of which are analyzed here: Typhoon Zeb on 15 October 1998 and Typhoon Xangsane on 31 October 2000.

For the typhoon Zeb flood flow simulation, the Manning roughness coefficients are first calculated by comparing the simulated results with the field-measured water levels at peak-flood discharge. The Manning roughness coefficients are initially given in the simulation domain based on the main river channel or floodplain regions [22]. In the main river channel, the Manning roughness coefficient is set to 0.025. In the floodplain, the Manning roughness coefficient is set to 0.05. Regarding boundary conditions, both sides of the vertical-walled levees along the simulation domain are considered as the land boundaries. A peak-flood discharge of $1800\,m^3/s$ in the Zeb typhoon is imposed at the subcritical inflow boundary and a field-measured water depth of 2.77 m is specified at the subcritical outflow boundary. As $t=0$, the velocity field is set to $u=0$, whereas the initial water level is set to 6 m in the entire computational domain. The time step is 0.03 s.

Table IV compares the simulated and the measured water levels at the six gauges after calibrating the Manning roughness coefficients. Good agreement is obtained at the E_1 norm for water level. Figures 9 and 10 present the simulated results under peak-flood condition to show the water-level

Table IV. Comparison of the measured data with the simulated water levels for flood flow simulations in the study reach.

	Typhoon Zeb			Typhoon Xangsane		
		Simulated (m)			Simulated (m)	
Gauges	Measured (m)	HRM	SGM	Measured (m)	HRM	SGM
G1	5.51	5.51	5.51	7.30	7.28	7.25
G2	3.80	3.76	3.64	5.39	5.35	5.35
G3	3.37	3.37	3.39	4.59	4.59	4.51
G4	4.66	4.81	4.54	6.49	6.52	6.31
G5	4.38	4.33	4.28	5.80	5.62	5.35
G6	3.52	3.56	3.32	4.65	4.69	4.62
	E_1 norm	1.10×10^{-2}	2.38×10^{-2}	E_1 norm	9.06×10^{-3}	2.43×10^{-2}

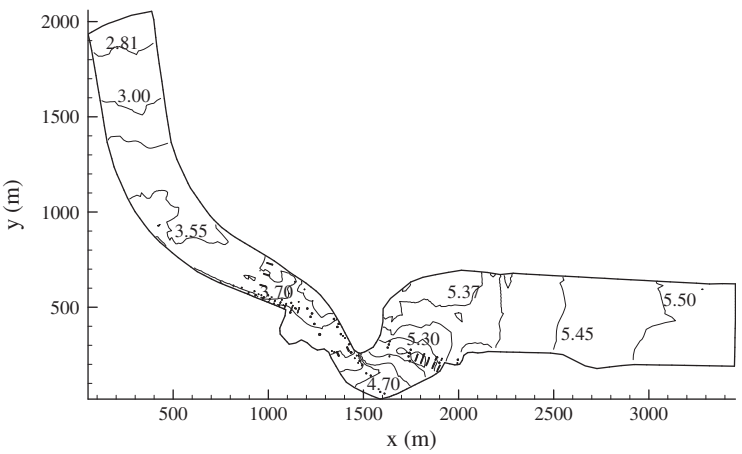

Figure 9. Simulated water-level contours in the Zeb typhoon flood flow simulation.

DOI: 10.1002/fld

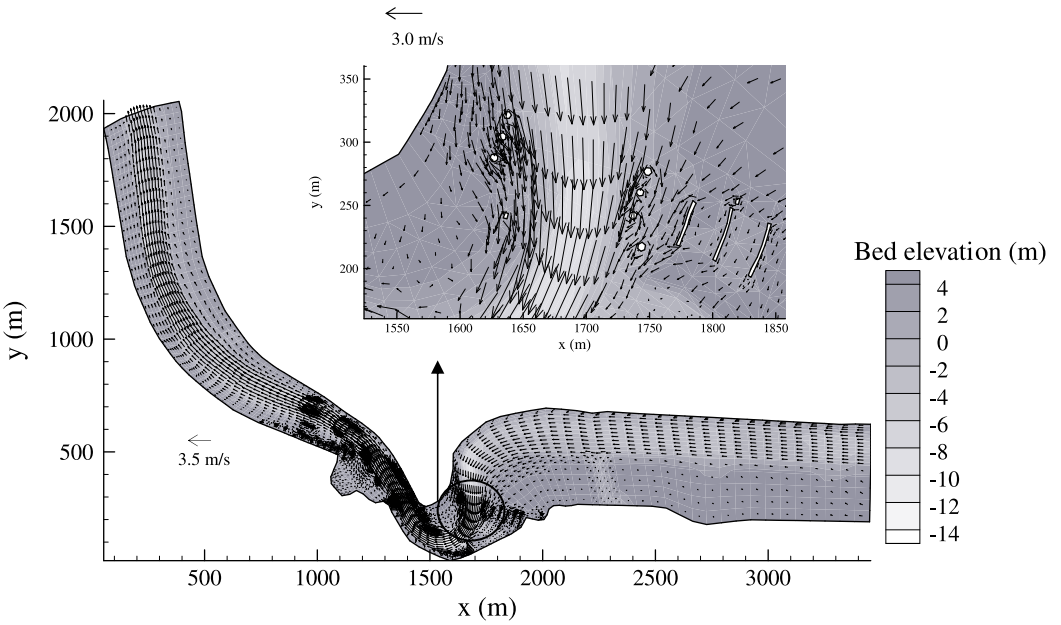

Figure 10. Velocity field in the Zeb typhoon flood flow simulation.

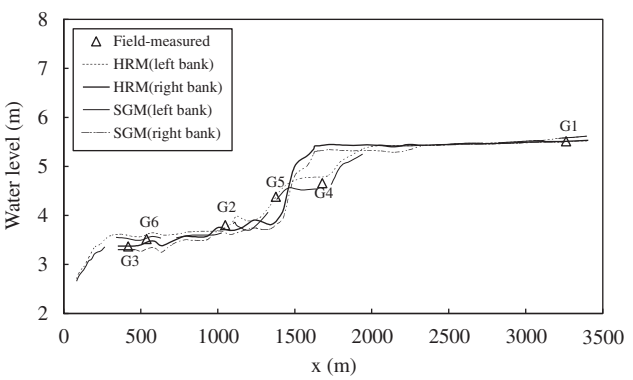

Figure 11. Comparisons of the field-measured and the simulated water levels along the left/right bank in the Zeb typhoon flood flow simulation.

contours and the velocity field, respectively. The close-up in Figure 10 shows that the major stream flow is confined along the main river channel, which indicates that the simulated velocity field is quite reasonable. Figure 11 shows the simulated water-level profiles along the left and right banks.

Second, flood flow during the Xangsane typhoon is simulated. The Manning roughness coefficients in the simulation domains are given by the calibrated results in the Zeb typhoon. A peak flow discharge of $2700\,m^3/s$ in the Xangsane typhoon is imposed at the subcritical inflow boundary and field-measured water depth of 4.2 m is specified at the subcritical outflow boundary. The initial conditions and the computational time step are the same as those in the flood flow simulation for

DOI: 10.1002/fld

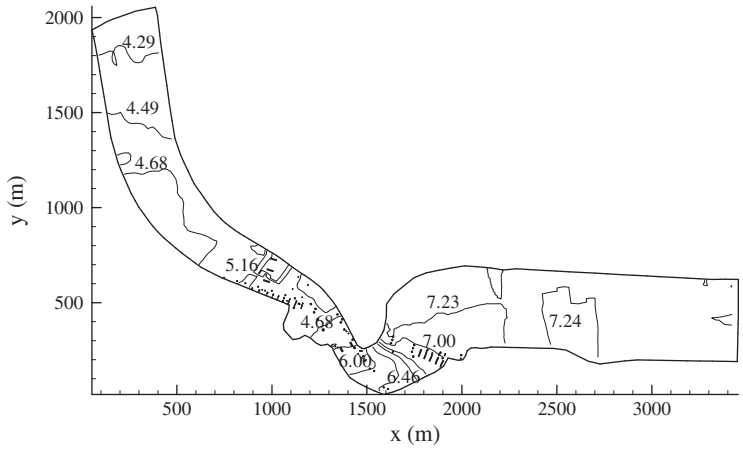

Figure 12. Water-level contours in the Xangsane typhoon flood flow simulation.

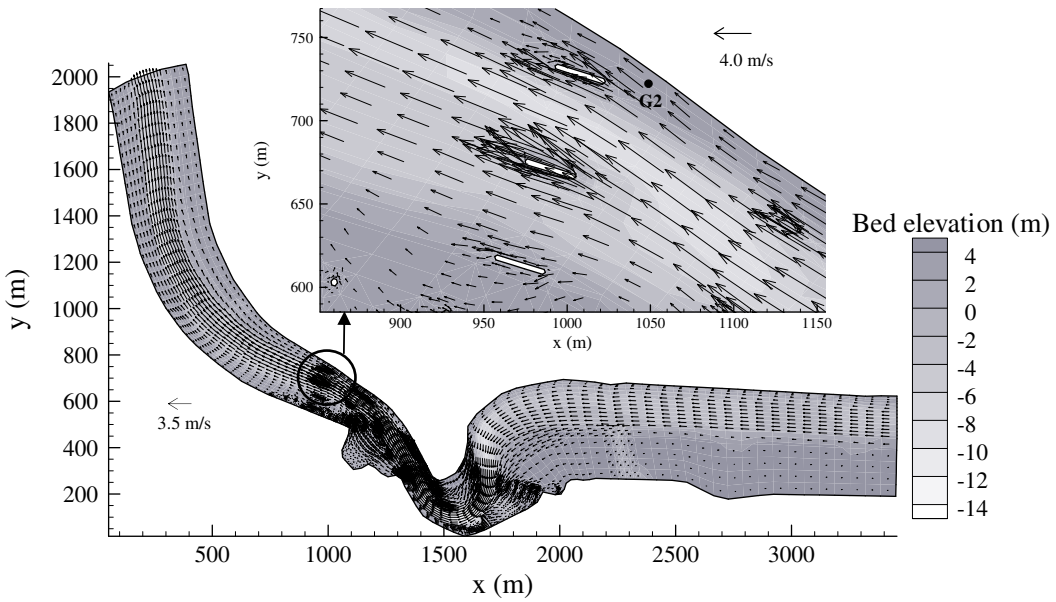

Figure 13. Velocity field in the Xangsane typhoon flood flow simulation.

Typhoon Zeb. Table IV compares the simulated water levels and measured readings from the six gauges. Figures 12 and 13 present the simulated results for water-level contours and velocity field, respectively, under peak-flood condition. Figure 13 demonstrates that the flow velocities in the main river channel are faster than those in the floodplain. Figure 14 shows the simulated water-level profiles along the left and right banks, which reveals good agreement with the measured data. In the close-up view of the area surrounding station G2, the local flow velocity tends to slow down in front of the bridge piers. Hence, the water levels along the right bank increase significantly

DOI: 10.1002/fld

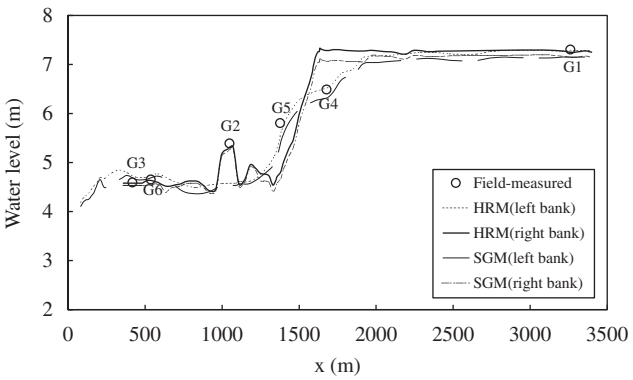

Figure 14. Comparisons of the field-measured and the simulated water levels along the left/right bank in the study reach for the Xangsane typhoon flood flow simulation.

due to bridge pier obstructions. The results by SGM are also plotted in Figure 14 for comparison with those by HRM. Table IV summarizes the E_1 error norms to quantitatively evaluate overall numerical accuracy. Clearly, the E_1 error estimates obtained for the flood flow simulations in the Zeb and Xangsane typhoons reveal the superior accuracy of HRM.

On the other hand, the stability test through numerical experiments is also performed herein. The maximum allowable time steps for the HRM and the SGM are 0.033 and 0.018 s, respectively. Hence, the HRM requires 60% less CPU time than the SGM.

5. CONCLUSIONS

The proposed well-balanced UFF scheme is extended to adequately balance flux gradients and source terms for shallow-water flow simulations with irregular bed topography. The new algorithm deals with the source terms using the HRM in the cell-centered finite-volume framework. The algorithm does not require the calculation of the Jacobian matrix that makes programming easier. The desirable well-balanced feature of the scheme is validated by simulating three benchmark problems and two flood flow simulations of a natural river.

The results of simulations indicate that both HRM and commonly used SGM can achieve steady-state solutions. In the 2D still-water flow test, the SGM produces spurious velocities, but the HRM does not. Compared with the SGM, the HRM consumes much less CPU time (up to 60%) with higher accuracy of the results.

The satisfactory results of the benchmark cases for model validation and real flood flow simulations for model application demonstrate that the proposed well-balanced UFF scheme is accurate, stable and efficient for practical hydraulic engineering analyses.

ACKNOWLEDGEMENTS

The authors would like to thank the National Science Council, Taiwan, for partially supporting this research under Grant No. NSC 96-2625-Z-002-013. The anonymous reviewers are appreciated for their valuable suggestions. Ted Knoy is appreciated for his editorial assistance.

DOI: 10.1002/fld

REFERENCES

1. Wang JW, Liu RX. A comparative study of finite volume methods on unstructured meshes for simulation of 2D shallow water wave problems. *Mathematics and Computers in Simulation* 2000; **53**:171–184.
2. Erduran KS, Kutija V, Hewett CJM. Performance of finite volume solutions to the shallow water equations with shock-capturing schemes. *International Journal for Numerical Methods in Fluids* 2002; **40**:1237–1273.
3. Wang JS, He YS, Ni HG. Two-dimensional free surface flow in branch channels by a finite-volume TVD scheme. *Advances in Water Resources* 2003; **26**:623–633.
4. Lin GF, Lai JS, Guo WD. Finite-volume component-wise TVD schemes for 2D shallow water equations. *Advances in Water Resources* 2003; **26**(8):861–873.
5. LeVeque RJ. Balancing source terms and flux gradients in high-resolution Godunov methods: the quasi-steady wave-propagation algorithm. *Journal of Computational Physics* 1998; **146**:346–365.
6. Hu K, Mingham CG, Causon DM. A bore-capturing finite volume method for open-channel flows. *International Journal for Numerical Methods in Fluids* 1998; **28**:1241–1261.
7. Zoppou C, Roberts S. Catastrophic collapse of water supply reservoirs in urban areas. *Journal of Hydraulic Engineering* 1999; **125**(7):686–695.
8. Erduran KS, Kutija V, Hewett CJM. Performance of finite volume solutions to the shallow water equations with shock-capturing schemes. *International Journal for Numerical Methods in Fluids* 2002; **40**:1237–1273.
9. Greenberg JM, Leroux AY. A well balanced scheme for the numerical processing of source terms in hyperbolic equation. *SIAM Journal on Numerical Analysis* 1996; **33**(1):1–16.
10. Gosse L. A well-balanced flux–vector splitting scheme designed for hyperbolic systems of conservation laws with source terms. *Computers and Mathematics with Applications* 2000; **39**:135–159.
11. Gallouet T, Herard JM, Seguin N. Some approximate Godunov schemes to compute shallow water equations with topography. *Computers and Fluids* 2003; **32**:479–513.
12. Kurganov A, Levy D. Central-upwind schemes for the Saint–Venant system. *Mathematical Modelling and Numerical Analysis* 2002; **36**:397–425.
13. Perthame B, Simeoni C. A kinetic scheme for the Saint–Venant system with a source term. *Calcolo* 2001; **38**(4):201–231.
14. Brufau P, Vazquez-Cendon ME, Garcia-Navarro P. A numerical model for the flooding and drying of irregular domains. *International Journal for Numerical Methods in Fluids* 2002; **39**:247–275.
15. Rogers BD, Borthwick AGL, Taylor PH. Mathematical balancing of flux gradient and source terms prior to using Roe's approximate Riemann solver. *Journal of Computational Physics* 2003; **192**:422–451.
16. Zhou JG, Causon DM, Mingham CG, Ingrams DM. The surface gradient method for the treatment of source terms in the shallow water equations. *Journal of Computational Physics* 2001; **168**:1–25.
17. Zhou JG, Causon DM, Ingrams DM, Mingham CG. Numerical solutions of the shallow water equations with discontinuous bed topography. *International Journal for Numerical Methods in Fluids* 2002; **38**:769–788.
18. Audusse E, Bouchut F, Bristeau MO, Klein R, Perthame B. A fast and stable well-balanced scheme with hydrostatic reconstruction for shallow water flows. *SIAM Journal on Scientific Computing* 2004; **25**(6):2050–2065.
19. Audusse E, Bristeau MO. A well-balanced positivity preserving 'second order' scheme for shallow water flows on unstructured meshes. *Journal of Computational Physics* 2005; **206**:311–333.
20. Lai JS, Lin GF, Guo WD. An upstream flux-splitting finite-volume scheme for 2D shallow water equations. *International Journal for Numerical Methods in Fluids* 2005; **48**(10):1149–1174.
21. Tan WY. *Shallow Water Hydrodynamics*. Elsevier: New York, 1992.
22. Chow VT. *Open Channel Hydraulics*. McGraw-Hill: New York, 1959.
23. Toro EF. *Shock-Capturing Methods for Free-Surface Shallow Water Flows*. Wiley: New York, 2001.
24. Lai JS, Lin GF, Guo WD. Simulation of hydraulic shock waves by hybrid flux-splitting schemes in finite volume method. *Journal of Mechanics* 2005; **21**(2):85–101.
25. Guo WD, Lai JS, Lin GF. Hybrid flux-splitting finite-volume scheme for the shallow water flow simulations with source terms. *Journal of Mechanics* 2007; **23**(4):399–414.
26. Guo WD, Lai JS, Lin GF. Finite-volume multi-stage schemes for shallow-water flow simulations. *International Journal for Numerical Methods in Fluids* 2008; **57**(2):177–204.
27. LeVeque RJ. *Finite Volume Methods for Hyperbolic Problems*. Cambridge University Press: Cambridge, U.K., 2002.
28. Tseng MH. Improved treatment of source terms in TVD scheme for shallow water equations. *Advances in Water Resources* 2004; **27**:617–629.

DOI: 10.1002/fld

29. Aureli F, Mignosa P, Tomirotti M. Numerical simulation and experimental verification of dam-break flows with shocks. *Journal of Hydraulic Research* 2000; **38**(3):197–206.
30. Brufau P, Garcia-Navarro P. Unsteady free surface flow simulation over complex topography with a multidimensional upwind technique. *Journal of Computational Physics* 2003; **186**:503–526.
31. Lai JS. Feasibility study on the raise elevation of the ZhongShan Bridge in the Keelung River—based on hydraulic data obtained from the physical modeling. *Research Report No. 441*, Hydrotech Research Institute, National Taiwan University, 2002 (in Chinese).

DOI: 10.1002/fld